ADVANCED MATERIALS
www.advmat.de

Nanoscale Operando Characterization of Electrolyte-Gated Organic Field-Effect Transistors Reveals Charge Transport Bottlenecks

Shubham Tanwar, Ruben Millan-Solsona, Sara Ruiz-Molina, Marta Mas-Torrent, Adrica Kyndiah, and Gabriel Gomila**

Charge transport in electrolyte-gated organic field-effect transistors (EGOFETs) is governed by the microstructural property of the semiconducting thin film that is in direct contact with the electrolyte. Therefore, a comprehensive nanoscale operando characterization of the active channel is crucial to pinpoint various charge transport bottlenecks for rational and targeted optimization of the devices. Here, the local electrical properties of EGOFETs are systematically probed by in-liquid scanning dielectric microscopy (in-liquid SDM) and a direct picture of their functional mechanism at the nanoscale is provided across all operational regimes, starting from subthreshold, linear to saturation, until the onset of pinch-off. To this end, a robust interpretation framework of in-liquid SDM is introduced that enables quantitative local electric potential mapping directly from raw experimental data without requiring calibration or numerical simulations. Based on this development, a straightforward nanoscale assessment of various charge transport bottlenecks is performed, like contact access resistances, inter- and intradomain charge transport, microstructural inhomogeneities, and conduction anisotropy, which have been inaccessible earlier. Present results contribute to the fundamental understanding of charge transport in electrolyte-gated transistors and promote the development of direct structure–property–function relationships to guide future design rules.

1. Introduction

Electrolyte-gated organic field-effect transistors (EGOFETs) are the building blocks for numerous sensing and bioelectronic applications[1] that include biorecognition[2,3] or electrophysiological recordings.[4,5] Recently, blends of organic small molecule semiconductors with insulating binding polymers have been considered as the active channel material, as they improve the solution processability and an enhanced microstructure crystallinity of the thin films, with well-defined crystalline domains. These improvements lead to devices exhibiting higher operational stability in comparison to the ones based on the bare semiconductor thin films.[6,7] However, understanding the thin film blended microstructure with two components and probing its impact on charge transport in operando across a range of length scales is challenging. Typically, in these blends, the organic semiconductor crystallizes on top of the bottom binding polymer layer,[8,9] while the charge transport layer is

S. Tanwar, R. Millan-Solsona, G. Gomila
Nanoscale Bioelectrical Characterization Group
Institut de Bioenginyeria de Catalunya (IBEC)
The Barcelona Institute of Science and Technology (BIST)
Carrer Baldiri i Reixac 11-15, Barcelona 08028, Spain
E-mail: gabriel.gomila@ub.edu

The ORCID identification number(s) for the author(s) of this article can be found under https://doi.org/10.1002/adma.202309767

DOI: 10.1002/adma.202309767

R. Millan-Solsona, G. Gomila
Department d'Enginyeria Electrònica i Biomèdica
Universitat de Barcelona
Carrer Martí i Franquès, 1, Barcelona 08028, Spain

S. Ruiz-Molina, M. Mas-Torrent
Institut de Ciència de Materials de Barcelona (ICMAB-CSIC)
Campus UAB Cerdanyola del Vallès
Barcelona 08193, Spain

A. Kyndiah
Center for Nano Science and Technology
Istituto Italiano di Tecnologia
Via Rubattino 81, Milano 20134, Italy
E-mail: adrica.kyndiah@iit.it

confined in a 2D channel top layer at the semiconductor/electrolyte interface,[10] since the semiconducting film is impermeable to ions. Therefore, the morphology and structure of the top layers of the semiconductor in contact with the electrolyte play a key role in the charge transport characteristics of these devices. In particular, the local charge transport is expected to be highly sensitive to grain boundaries and orientation of different crystalline domains that, under applied biases, absorb significant potential drops and funnels the charge carriers anisotropically to different domains, creating inhomogeneous charge distributions and thus negatively impacting the overall device effective charge carrier mobility.[11,12] The semiconductor/electrolyte interface, in addition, can present nanoscale interfacial heterogeneities due to additional vertical phase separation phenomena of blended components[6,7,9,13] leading to ultrathin (≈1 nm) skin dielectric layers of the insulating binding polymers that directly influence the local charge carrier density.[14] Therefore, determining the critical aspects of the device's microstructure and its influence on various charge transport parameters, such as charge carrier mobility, contact access resistances, inter- and intradomain charge transport, and conduction anisotropy, is essential for creating stable and high-performance materials for EGOFET devices. In this regard, operando scanning-probe-microscopy-based techniques offer a unique capability to probe these characteristics over a broad range of scales (from nano- to micrometer device scales) and to reveal how different transport paths through the device microstructures are coupled together and linked with the overall device performance.

In the case of solid-state organic field-effect transistors (OFETs), Kelvin probe force microscopy (KPFM) is a widely used technique in air or vacuum environment for measuring the local electric potential distribution and charge trapping dynamics that allow extracting relevant charge transport parameters for establishing structure–function relationships.[15–17] However, the conventional KPFM technique cannot operate in aqueous electrolytes due to strong DC and low-frequency AC-bias-induced charge screening dynamics and electrochemical processes, prohibiting direct access to local electrical properties in devices like EGOFETs.[18] Recently, in-liquid electrical scanning probe techniques such as scanning electrochemical microscopy (SECM)[19] and in-liquid scanning dielectric microscopy (in-liquid SDM)[14] have been proposed as viable options to address the local electrical properties of such devices as the probe can be located above the semiconducting channel at the electrolyte/semiconductor interface and thereby can directly probe the local electrical properties. Mariani et al. used SECM to measure the electrochemical potential relative to the quasi-reference-electrode in millimeter-sized operating organic electrochemical transistors, enabling microscopic determination of charge carrier density and mobility.[19] However, this technique has limited applicability due to low spatial resolution because of the micrometric size of the SECM probe, thereby requiring device channel footprints that are far from the application-relevant scale. On the other hand, Kyndiah et al.[14] recently implemented in-liquid SDM for nanoscale mapping of the electrical properties (conductivity and interfacial capacitance) in operating EGOFETs via measurement of local electrostatic forces. The measured electrostatic forces were converted to maps of local conductivity and interfacial capacitances using finite element modeling approaches.[14] However, a comprehensive understanding of charge carrier transport at the nanoscale under different operating conditions and microstructural thin film arrangements has not been addressed, primarily because of fundamental and technical challenges in accessing certain electrical properties, specifically the local electric potential in a liquid electrolyte environment, and secondarily due to the technical difficulty in gaining quantitative information at high throughput. The latter limitation was recently overcome by developing an automated high throughput in-liquid SDM setup for the operando nanoscale electrical characterization of electrolyte-gated transistors that allows exploring a wide range of gate and drain voltages.[20] The former primary fundamental limitation related to the potential mapping in operating EGOFETs is addressed and solved here in the present work.

In this work, we investigated the structure–electrical property–function relationships in operating EGOFETs across all operational regimes (subthreshold, linear, and saturation) using a robust interpretation framework of in-liquid SDM that effectively circumvented the current challenge of using KPFM in liquid. We demonstrate that the local electric potential can be quantitatively mapped directly from raw experimental electrostatic force data without requiring calibration or numerical simulations, facilitating straightforward nanoscale assessment of the various charge transport bottlenecks. Based on this development, we revealed the role of the microstructural arrangement of the organic semiconductor thin film on the device performance across all operational regimes and provided a direct comprehensive picture of the charge carrier transport at the nanoscale. Additionally, supported by finite-element simulations, we revealed the anisotropy in the charge carrier transport, which displays a much higher conductivity in the longitudinal direction along the channel than in the transversal direction, and which has significant implications on the access series resistance values and the performance of the transistor operation.

2. Results and Discussion

We investigated a solution processed EGOFET based on a blend of the organic semiconducting material 2,8-difluoro-5,11-bis(triethylsilylethynyl) anthradithiophene (diF-TES-ADT) and the insulating polymer polystyrene (PS).[21] Previously, we have used these films to engineer EGOFETs as stable bioelectronic recording platforms for excitable cells,[5] for the development of biosensors[22] and as a test platform to demonstrate the capabilities of in-liquid SDM.[14] The structure–property relationships of this material in solid-state OFETs have been studied with different techniques,[16,23] thus providing the foundation for corroborating the findings in EGOFETs.

2.1. Macroscale Characterization of EGOFETs

The schematic of the measurement approach for both global and local operando characterization of EGOFETs is shown in **Figure 1a**. The SDM conductive probe is biased with an amplitude-modulated high frequency (megahertz) waveform (V_{AM}), which is offset by a DC gate voltage (V_{GS}) equal to the one

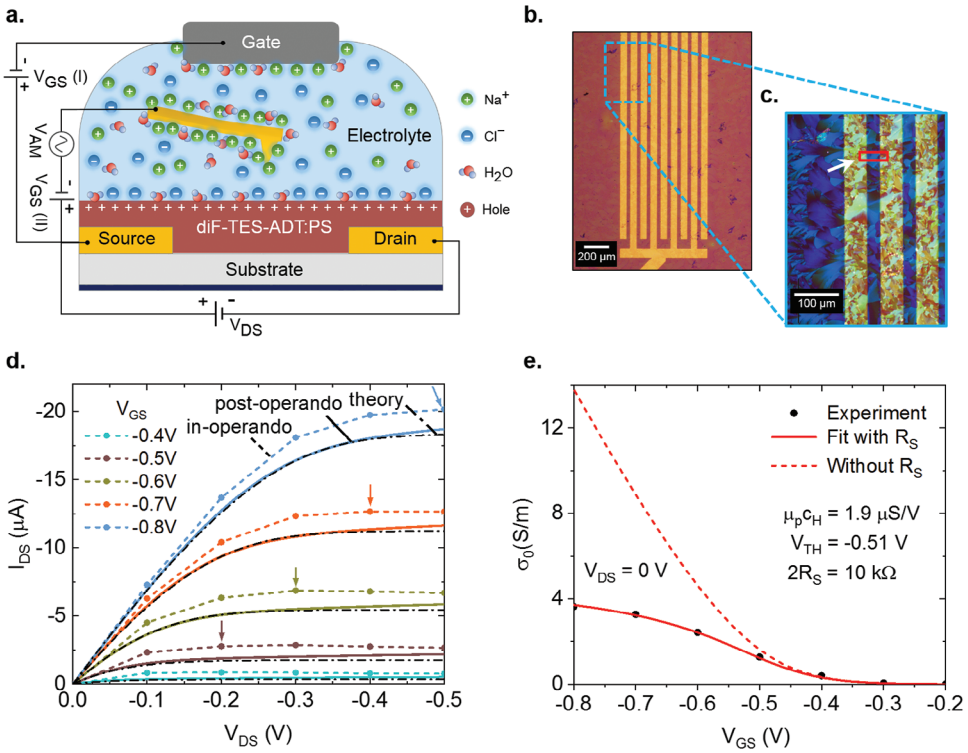

Figure 1. Macroscale characterization of EGOFETs. a) Schematics of the simultaneous local and global characterization of operando EGOFETs in an electrolyte (concentration 1 mM of NaCl) solution by in-liquid SDM. b) Optical microscopy image of the interdigitated device with nominal channel length $L = 30$ µm, width $W = 19\,680$ µm ($W/L = 656$), and thickness $h_{sem} = 30$ nm. c) Polarized light microscopy image of the region marked with a blue rectangle in (b). The region marked with the red rectangle and highlighted by the white arrow indicates the location where in-liquid SDM local measurements were done in this device. d) (continuous lines) Output *I–V* characteristics of one of the EGOFET analyzed in the present study measured post operando after the full set of in-liquid SDM measurements. (symbols) Average drain current measured during the operando in-liquid SDM measurements. (dotted-dashed line) Fitting with the Helmholtz model of the experimental *I–V* considering series resistance effects. The arrows indicate the approximate voltage V_{DS} at which the current saturates. e) (symbols) Device conductivity at $V_{DS} = 0$ V obtained from the *I–V* output curves as a function of V_{GS}. (continuous line) Prediction of the Helmholtz model including series resistance with the parameters extracted in (d). (dashed line) Effective semiconductor conductivity at $V_{DS} = 0$ V obtained by subtracting the effect of series resistance.

applied to the external platinum gate electrode. The amplitude-modulated waveform applied to the SDM probe leads to a modulated static bending of the cantilever due to the resulting electrostatic force, which depends on the local electrical properties of the material underneath at the measuring frequencies (megahertz).[14] The use of frequencies above the dielectric relaxation frequency of the electrolyte is crucial to stabilize the interfacial ionic diffusive layer, preventing it from fluctuating and absorbing the ac potential applied to the tip, and hence making the electric force insensitive to the dynamic properties of the ionic diffusive space charge layer.[14] Additionally, a voltage V_{DS} is applied between the source and drain electrodes leading to the current I_{DS} flowing through the device, which is also measured. Figure 1b,c shows optical microscopy images of the device with and without a polarizer, respectively. The device consists of interdigitated source–drain electrodes with a channel length $L = 30$ µm, an effective channel width $W = 19680$ µm ($W/L = 656$), and a nominal semiconductor thickness $h_{sem} = 30$ nm. The device geometry has been optimized for the applications of these EGOFETs as biosensing and bioelectrical recording platforms.[5,22] The contrast in the polarized optical microscopy image results from the birefringence of the semiconducting material, depicting the heterogeneity due to different orientations of the crystalline domains that originate from the pentafluorobenzenethiol (PFBT)-coated electrode surface and interleave in the channel area.[16]

The underlying source–drain electrodes provide a brighter contrast in the polarized images. The presence of well-defined domain boundaries in the channel area was observed also in previous studies and is typical for these type of materials.[7,16,21,23] The present study aims to understand how these heterogeneous structures and morphology impact the interfacial charge transport at the electrolyte/semiconductor interface.

Figure 1d (continuous lines) shows the output characteristics of the device in a 1 mM NaCl aqueous solution measured under the same configuration as used later for the nanoscale electrical measurements with in-liquid SDM. The output *I–V* characteristics show the typical behavior of EGOFETs depicting subthreshold, linear, and saturation regimes and can be described quantitatively using our recently proposed analytical EGOFET Helmholtz model considering series resistance effects.[24] The Helmholtz's model assumes a voltage-independent electrolyte dielectric layer capacitance, thus indicating that in the devices studied, the voltage dependence of the interfacial ionic diffusive space charge layer does not play a significant role. The model perfectly fits the output characteristics, as shown with the dotted-dashed lines in

Figure 1d, providing the following device parameters: intrinsic threshold voltage without series resistance effect $V_{TH} = -0.51$ V, mobility–capacitance product $\mu_p c_H = 1.9$ μS V^{-1} and series resistance $R_s = 5$ kΩ. The mobility–capacitance product agrees well with the values reported in the literature,[25] indicating an acceptable level of intrinsic performance despite a relatively large threshold voltage. The series resistance probably stems from the staggered configuration of the device,[24] the polycrystalline nature of the semiconducting thin film material, the vertical phase separation of the semiconductor and the insulating layer, and the low transversal conductivity of this material owing to inferior out-of-plane π-orbital overlap[23] leading to high access resistance, as we will show later from the nanoscale SDM measurements.

Figure 1e (black dots) shows the effective device conductivity calculated from the output characteristics at $V_{DS} = 0$ V as $\sigma_0(V_{GS}) = (L/Wh_{sem})\partial I_{DS}/\partial V_{DS}|_{V_{DS}=0\ V}$. The continuous red line represents the prediction of the Helmholtz model considering the series resistance effect,[24] which is in excellent agreement, while the dashed red line indicates the effective semiconductor channel conductivity after suppressing series resistance effects. The effective channel conductivity reaches >10 S m^{-1}, showing a readily remarkable value for a polycrystalline material, which is at the basis of the robust performance of these EGOFETs.[5,22]

2.2. Nanoscale Probing of Different Operating Regimes of EGOFETs by In-Liquid SDM

In-liquid SDM measurements were performed by means of an automated setup recently developed (see the Experimental Section and Ref. [20]) with a much-improved throughput as compared to our earlier approach.[14] Nanoscale measurements were performed on the region marked with a red rectangle and white arrow in Figure 1c. At each pixel in the scan region, approach curves of the cantilever deflection and oscillation amplitude were measured, from which topographic and local electrostatic force images were constructed. The measured electrostatic force encodes the information about electrically relevant local properties like conductivity and compact interfacial capacitances, which are generally extracted by modeling the tip–sample interactions using the finite element method after following the appropriate data calibration procedure.[14,26] **Figure 2a** shows a zoomed version of the polarized light microscopy image of the region analyzed (64 × 16 μm^2) spanning a source–channel–drain area, where different crystalline domains of the semiconductor thin film are distinctly visible. The choice of this specific region for local measurements is based on its composition, which includes a homogeneous top section comprising a single crystalline domain linking the source and drain electrodes (upper ≈4 μm segment of the image) and a bottom region where multiple domains intersect (lower ≈12 μm segment of the image). Figure 2b shows the topographic image of the same region, showing relatively uniform thin-film morphology with few structural features matching the optical polarization image in Figure 2a highlighted by the black, red, and white arrows. Notably, not all structural features displayed in the polarized optical image give rise to topographic variations. The height difference between the channel and electrodes is ≈ 55 ± 10 nm, as depicted by the superimposed cross-section profile, in reasonably

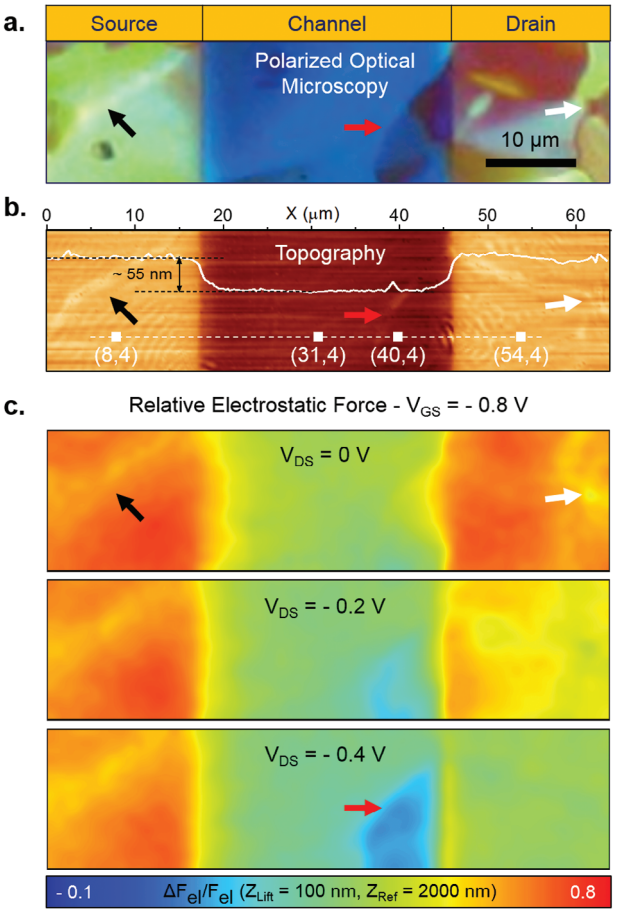

Figure 2. Revealing microstructure impact on transport with local electrostatic forces. a) Polarization light microscopy image of a 64 × 16 μm^2 area of the EGOFET transistor (red rectangle region with white arrow in Figure 1c), including source, channel, and drain regions. b) AFM topography of the same area as in (a) with the topographic profile superimposed. c) Relative electrostatic force lift-mode images (Z_{lift} = 100 nm and Z_{ref} = 2000 nm) for $V_{GS} = -0.8$ V and $V_{DS} = 0$, −0.2, and −0.4 V. Experimental parameters for in-liquid SDM measurements: electrolyte = 1 mM NaCl, gate = Au SDM probe (HQ:NSC19/Cr–Au) + Pt external electrode, f_{el} = 25 MHz, f_{mod} = 10 kHz, $V_{ac} = 2$ V_{PP}, pixels 64 × 16, $k = 1.097$ N m^{-1}, f_{res} = 34.90 kHz (cantilever).

good agreement with the nominal thickness of the electrodes (≈ 45 nm). Figure 2c shows lift-mode relative electrostatic force images with $Z_{lift} = 100$ nm and $Z_{ref} = 2000$ nm, for $V_{GS} = -0.8$ V and $V_{DS} = 0$, −0.2, and −0.4 V. In the present work, following Ref. [20], we use relative electric force variations rather than absolute values,[14] as it provides significant advantages and accurately captures the local trends by effectively removing high-frequency artefacts (see the Experimental Section and Ref. [20]).

As we mentioned above, the variations measured in the local (relative) electrostatic force as a function of bias voltages are directly related to local conductivity variations, since the local conductivity is the sole sample electrical property affected by bias voltages that directly affects the electrostatic force. Due to the high frequency (megahertz) of SDM measurements, above the dielectric relaxation frequency of the electrolyte, the interfacial diffuse ionic layer does not fluctuate and hence its capacitance

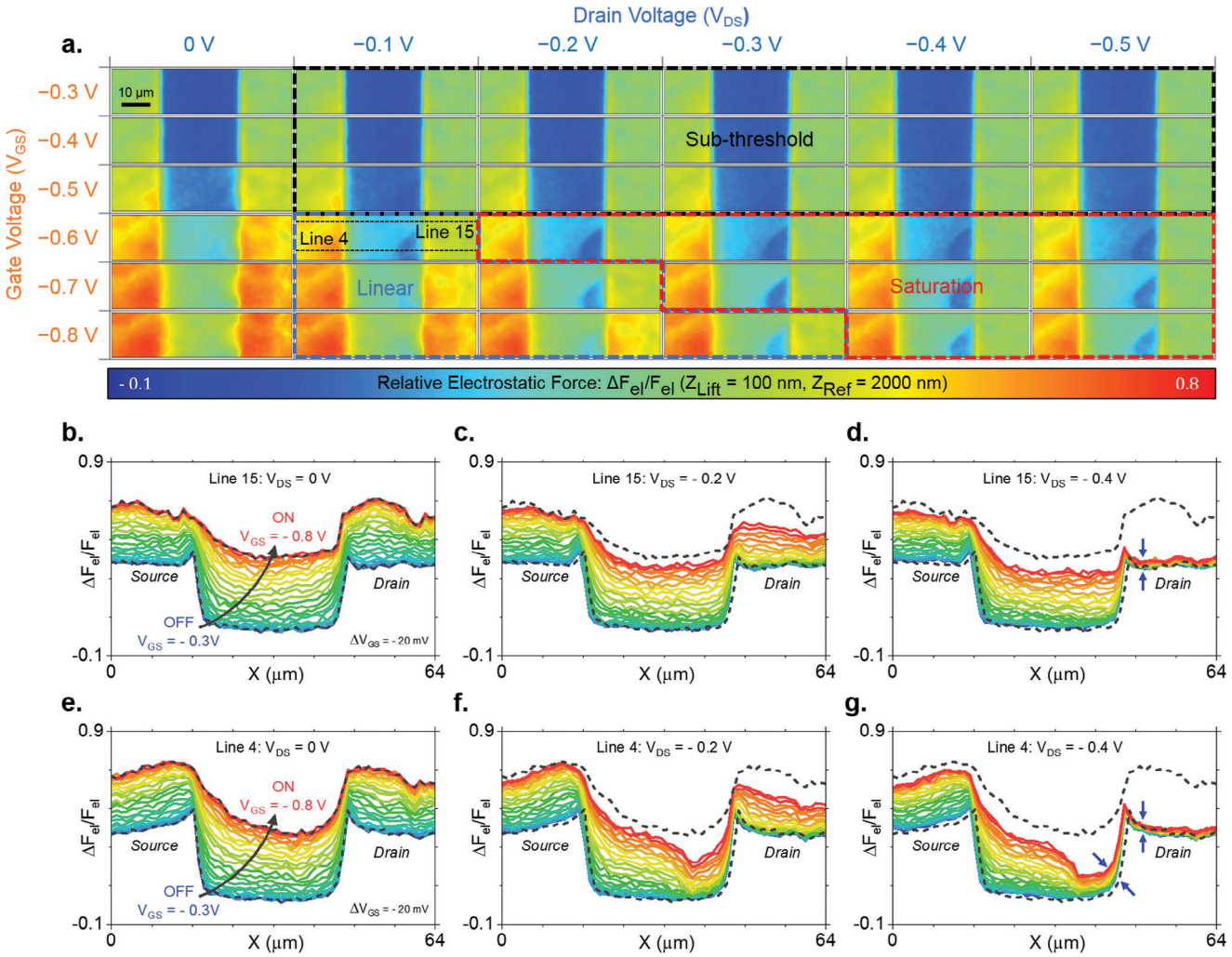

Figure 3. Nanoscale probing of different operating regimes of an EGOFET by in-liquid SDM. a) Lift-mode relative electrostatic force images (Z_{lift} = 100 nm and Z_{ref} = 2000 nm) for V_{GS} and V_{DS} voltages covering all operating regimes, which are highlighted by the thick dashed lines (black for subthreshold, blue for linear, and red for saturation regime). The scale bar corresponds to 10 µm. b–d) Relative electrostatic force profiles along scan line 15 for the different V_{GS} and for V_{DS} = 0, −0.2, and −0.4 V, respectively. e–g) Idem for scan line 4. The location of scan lines 4 and 15 is shown in (a) for V_{DS} = −0.1 V and V_{GS} = −0.6 V. The black dashed profiles in (b–g) represent the sensitivity limits of the electrostatic force on the local conductivity for high (top line) and low (bottom line) conductivities. Experimental parameters are the same as in Figure 2.

is not directly detected through the electric force measurement at megahertz frequencies, while the Stern interfacial capacitance generally remains constant as a function of bias voltages. Furthermore, we did not observe any relevant variation in the topography of the semiconductor thin film obtained simultaneously to the electrical images (see Figure S1 in the Supporting Information), discarding relevant modification in its microstructure due to its interaction with the electrolyte and variations in applied voltages. A noticeable contrast between the source/drain and channel regions is observed in the measured electrostatic force maps, attributed to the underlying substrate (metal electrode vs an insulating substrate), as discussed elsewhere.[14] At zero drain voltage (V_{DS} = 0 V), the electrostatic force image appears symmetrical, as both the source and drain display similar values (top image in Figure 2c). Contrarily, increasing the drain voltage introduces an asymmetry in the electrostatic force distribution (middle (V_{DS} = −0.2 V) and bottom (V_{DS} = −0.4 V) images in Figure 2c), resulting in lower values at the drain, representing lower local conductivities,[14] which is compatible with the presence of space charge transport, characteristic of FET devices. Additionally, some of the microstructural features of the material become apparent as the drain voltage increases, particularly in the channel region where the presence of a grain only manifests at relatively high drain voltages (red arrow in the bottom image in Figure 2c). These results show that electrostatic force images can reveal the inhomogeneous conductivity distributions along the channel and microstructure material effects when measured in operating EGOFETs.

Figure 3a shows the nanoscale evolution of the electrostatic force images as a function of drain and gate voltages, encompassing subthreshold, linear, and saturation regimes. Only a subset of the more than 300 images acquired is shown here due to limited space, while the complete dataset is available in Figure S1 (Supporting Information). Figure 3b–d (res. Figure 3e–g shows

relative electrostatic force image profiles along scan line 15 (res. scan line 4) for different V_{GS} (−0.3 to −0.8 V in steps of 0.02 V) and $V_{DS} = 0$, −0.2, and −0.4 V, respectively. Scan line 15 traverses the region where a single crystalline domain bridges the source and drain, while scan line 4 traverses an area containing intersecting crystalline domains (see the location of the scan lines in Figure 3a for the case of $V_{DS} = -0.1$ V and $V_{GS} = -0.6$ V). The different transport regimes in Figure 3a are denoted with thick dashed lines overlaying the images according to the output I–V characteristics shown in Figure 1d. In the subthreshold regime, the conductivity is too low to be detected in the SDM measurements; therefore, the measured electrostatic force reflects the interaction of the conductive tip with an insulating material and thus stays low. As the gate voltage surpasses the threshold voltage, the conductivity is high enough to be detected by the SDM probe. When $V_{DS} = 0$ V, the force increases uniformly across the device with increasing gate voltage, as shown in Figure 3b,e. The black dashed lines in Figure 3b,g correspond to the condition where the electric force becomes insensitive to the local conductivity, either because it is too high (top dashed line) or too low (bottom dashed line). The application of a drain voltage in the linear regime leads to an asymmetry in the spatial distribution of the electrostatic force along the channel, with its value decreasing toward the drain electrode, see Figure 3c,f, as pointed out above. For high enough drain voltages, the electrostatic force over the drain is not modulated by the gate voltage any further and takes values similar to the subthreshold regime, indicating a local off-state and denoting the occurrence of a pinch-off in the saturation regime, as shown in Figure 3d,g. An important observation is that electrical features correlating with the polycrystalline microstructure of the semiconductor film start appearing in the channel with increasing drain voltages, as also pointed above. Surprisingly, the local extension of the pinch-off in the channel can be promoted by the semiconductor microstructure, as indicated by the blue arrows in Figure 3g for scan line 4. By contrast, for scan line 15 in Figure 3d, the pinch-off is mostly restricted only to the drain electrode.

Similar measurements were performed on various devices and regions exhibiting unique multiscale structural features to comprehensively assess the diverse influence they have on the evolution of local electrical properties. For instance, Figure S2 (Supporting Information) shows the case where the Atomic Force Microscopy (AFM) topography of the grain boundary consists of a pattern of open gaps and closed smooth boundaries between adjacent grains, topographically similar to the one reported for the diF-TES-ADT and poly(triarylamine) (PTAA) blend thin film.[27] In this case, the microstructure is visible at high drain voltage, although subtle compared to the one in Figure 3, representing a moderately restricting grain boundary. Figure S3 (Supporting Information) shows a subtle grain boundary effect at intermediate gate voltages; however, a pronounced impact is observed at high gate voltages with a sudden massive drop at the grain boundary, even for $V_{DS} = 0$ V. Figure S4 (Supporting Information) illustrates a case where part of the channel is decorated with 3D textured crystallites, suspected in the literature to be detrimental to charge transport;[16] indeed, we observed that the electrostatic force evolution in this region is limited as a function of gate voltage compared to the homogenous region. Finally, Figure S5 (Supporting Information) illustrates the impact of the orientation of the grain boundaries with respect to the source and drain electrodes. Grain boundaries parallel to the current path bridging the source and drain electrodes show relatively little impact in the electric force distribution, while grain boundaries perpendicular show an important detrimental effect. Therefore, formulating the device fabrication strategy that results in a particular dominating orientation of the crystalline domain across the device area could improve its characteristics.

The above results demonstrated the impact of diverse structural signatures on the evolution of the local conductive properties of the device in operando, including on the extension of the pinch-off into the channel. If a single domain exists between the source–drain electrode, the pinch-off is mostly limited to the drain electrode. However, if there are multiple domains, the pinch-off may extend to the channel, with the extent depending on the distribution of the grains.

2.3. Local Potential Mapping of Operating EGOFETs

In order to provide a quantitative evaluation of the influence of the thin film microstructure and heterogeneity on the device performance, it would be desirable to map the local electric potential distribution within the source–channel–drain region, similar to what is done with conventional KPFM in solid-state OFETs.[15–17] Since conventional KPFM cannot be operated in the aqueous electrolyte environment, we have developed a novel strategy to achieve it.

To map the local electric potential from the local electrostatic forces measured by in-liquid SDM, we took advantage of the dependence of the local conductivity on the local electric potential. We assumed that i) the voltage dependence of the local electrostatic force at a given position (x, y) is univocally determined, to a good approximation, by the local semiconductor sheet conductivity, i.e.

$$F_{elec}\left(x, y, z; V_{GS}, V_{DS}\right) = F\left[\sigma\left(x, y; V_{GS}, V_{DS}\right), z\right] \quad (1)$$

and that ii) the local conductivity in the on-state at nonzero V_{DS} can be related to a good approximation to the conductivity at zero source–drain voltage evaluated at the local effective gate voltage, $V_{GS}' = V_{GS} - V(x, y)$, i.e.

$$\sigma\left(x, y; V_{GS}, V_{DS}\right) = \sigma_0\left[x, y; V_{GS} - V\left(x, y; V_{DS}\right)\right] \quad V_{DS} < 0 \quad (2)$$

where, $V(x, y)$ is the local potential drop along the channel at position (x, y) for the given V_{GS} and V_{DS}. Under these assumptions, which are reminiscent from the gradual channel approximation used in the modeling of field-effect transistors,[28] one has

$$F_{elec}\left(x, y, z; V_{GS}, V_{DS}\right) = F_{elec,0}\left[x, y, z; V_{GS} - V\left(x, y; V_{DS}\right)\right] \quad (3)$$

i.e., the local electrostatic force measured at a given position (x, y) and bias potentials (V_{GS} and V_{DS}) is equal to the local electrostatic force measured at the same position for $V_{DS} = 0$ V and at the local effective gate potential $V_{GS}' = V_{GS} - V(x, y)$. Therefore, the local electric potential $V(x, y)$ at a given V_{GS} and V_{DS} can be obtained by comparing the (relative) electrostatic force measured at these voltages with those measured at $V_{DS} = 0$ V and identifying the

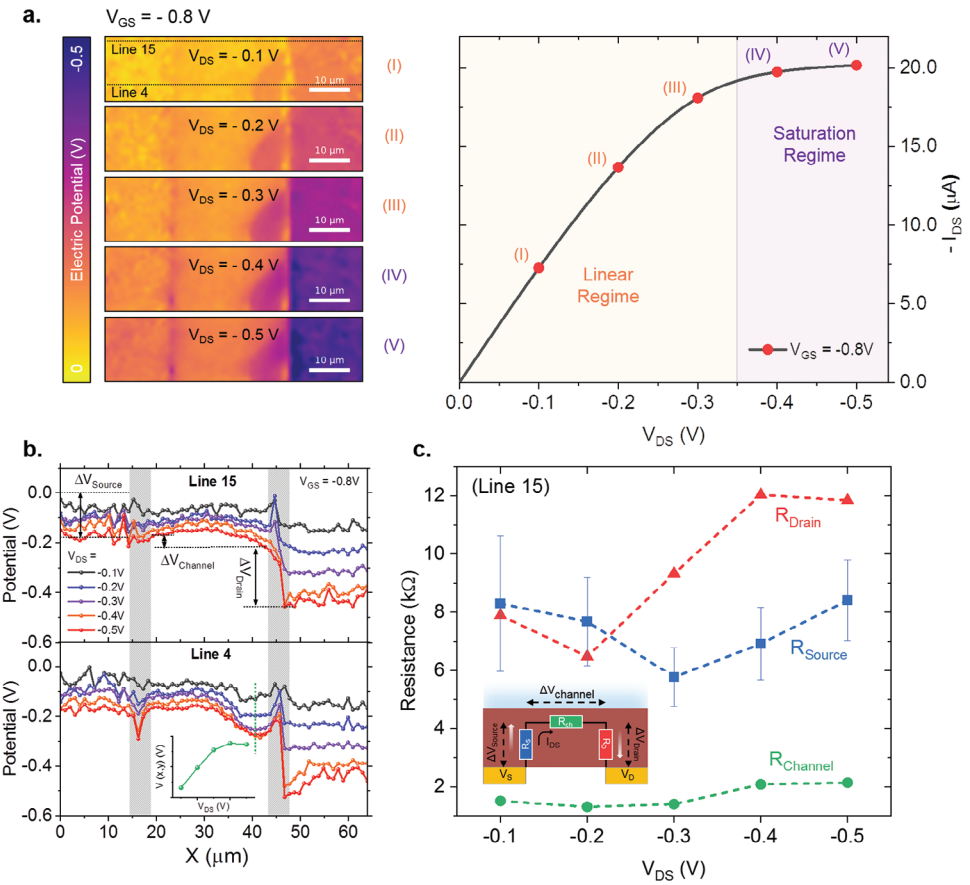

Figure 4. Local potential mapping of an operating EGOFET. a) Electric potential maps $V(x, y)$ corresponding to $V_{GS} = -0.8$ V and V_{DS} varying from −0.1 to −0.5 V. Each map is linked to the corresponding point in the associated output I–V curve for $V_{GS} = -0.8$ V. b) Potential profiles along the dashed lines in (a) corresponding to scan lines 15 and 4. Inset in scan line 4 graph shows the local potential evolution in the crystalline domain attached to the drain electrode at the location highlighted by the dotted green line. The stripped gray regions in the background represent source/channel and channel/drain interfaces. c) Resistances associated with source, channel, and drain ($R = \Delta V/I_{DS}$) calculated as a function of drain voltage obtained from the potential profiles for the scan line 15 in (b) with ΔV highlighted for source, channel, and drain. The error bars for the source curve are derived from the standard deviation of the electric potential over the source region. In the channel and drain regions, the calculation is done using only two data points across their respective lengths/interfaces, so error bars are not plotted. Inset: schematic of the charge carrier transport path from source to drain with different resistances and voltage drops identified.

gate potential shift that make them equal (see the Experimental Section and Figure S6 in the Supporting Information).

Figure 4a shows the local electric potential maps obtained following this procedure for $V_{GS} = -0.8$ V and V_{DS} varying from −0.1 to −0.5 V, spanning linear to saturation regimes as defined in the associated output I–V curve (see Figure S6 in the Supporting Information for the potential maps for all drain and gate voltages).

Figure 4b shows the potential profiles along scan lines 15 and 4, representing, respectively, regions with single and multiple active grains in the channel region, as mentioned before. For scan line 15, most of the potential drops at the contacts so that the electric potential in the channel looks relatively uniform for low V_{DS} (the small slope leading to the local electric field is not detectable), while it develops a significant nonlinearity at higher V_{DS}, consistent with the development of a space charge limited transport in the semiconductor. On the contrary, in scan line 4, the potential drops mostly at the contacts and at the grain boundary, with only a very small drop occurring in the remaining part of the channel. In particular, the local voltage in the channel grain connected to the drain electrode increases and then saturates with increasing drain voltage (see inset of Figure 4b for scan line 4), thus leading to the extension of the pinch-off into the channel region. The above results show that the crystalline domains show excellent conductive properties with minimal voltage drop within them, while grain boundaries and contacts absorb most of the applied potential, hence severely reducing the performance of the device.

The following picture emerges from the previous analysis: for zero drain voltage and increasing gate voltages, the channel is formed at the electrolyte/semiconductor interface that also occupies the area above the electrodes and all the grains present in the channel. Then, as the drain voltage increases, the electric potential starts redistributing according to the presence of grain boundaries, space charge effects, and contact effects, thereby changing locally the conductivity. For instance, the area above the drain starts depleting, and the applied drain voltage defines the local potential over the drain electrode. Similarly, at some grain boundaries, significant drops in potential may occur, resulting in the

depletion of some of the grains and giving rise to low conductivity grain regions, which were, instead, highly conductive at low drain voltages. Finally, we note that the potential on the source electrode (which is at ground) slightly decreases as the drain voltage is increased. This fact can be due to the presence of series resistance effects (R_{source}) since the charge carriers need to travel from the source to the conduction channel, and hence face the source contact resistance that includes the charge injection resistance at the source/semiconductor interface and the semiconductor bulk transversal access resistance (see inset in Figure 4c). After reaching the channel, the charge carriers traverse the channel ($R_{channel}$) and reaches the drain electrode edge (R_{drain}) following the least resistance path (see inset Figure 4c). Figure 4c shows the different resistances determined from the electric potential profiles for scan line 15 ($R = \Delta V/I_{DS}$), as a function of drain voltage. The source resistance remains relatively constant as a function of drain voltage ($R_S \approx$ 6–8 kΩ), and its magnitude is consistent with the one obtained from the Helmholtz model fitting at $V_{DS} = 0$ V depicted in Figure 1e where $R_s = 5$ kΩ. On the other hand, the drain resistance R_D initially shows a value similar to R_S for low drain voltages but later it shows significant drain voltage dependence, thereby absorbing most of the potential drop at high drain voltages and prohibiting the pinch-off from extending into the channel, as observed in Figure 3d. A similar lack of pinch-off in the channel due to the strong dependence of the drain resistance on drain voltage is reported in the n-type OFETs based on N,N'-bis-(1H,1H-heptafluorobutyl)-1,7-dicyanoperylene-3,4:9,10-tetracarboxylic diimide (PDI-FCN_2) in the limiting case of a thin (6 nm) semiconducting layer using gated four-probe measurements.[29] The relatively low channel resistance in the homogeneous section (scan line 15) suggests efficient intradomain charge transport. However, significant voltage drops at the contacts and grain boundaries act as bottlenecks for charge transport.

2.4. Conduction Anisotropy

The PFBT-treated source–drain electrodes are known to enforce <001> crystallites of the diF-TES-ADT, where molecules pack cofacially with their aliphatic side chains oriented perpendicular to the substrate.[23,27] The <001>-textured film exhibits optimal in-plane π-stacking, benefiting longitudinal charge carrier transport in the transistor channel. However, this arrangement reduces out-of-plane π-orbital overlap and thus suppresses transversal charge carrier transport over the electrodes. This conduction anisotropy has significant implications for the injection/extraction of charge carriers into/from the transistor channel. In-liquid SDM measures the electrostatic forces between the tip and the sample. Since electrostatic forces are long-ranged, they probe a certain volume of the material under study, which in the case of the semiconductor thin films of the EGOFETs of the present study (≈30 nm thick) comprises the whole semiconductor thickness. Therefore, in-liquid SDM can probe the conduction anisotropy, since it probes the transversal conductivity ($\sigma_\perp$) when the probe is on the electrodes, due to the presence of a metallic substrate, whereas it probes mainly the longitudinal ($\sigma_\parallel$) conductivity when in the channel, due to the presence of the insulating substrate (see Figure S8 in the Supporting Information). The quantitative analysis of the local conductivity in four locations along the scan line 4, highlighted in Figure 2b, has been carried out by using the numerical model presented elsewhere[14] (see Figure S9 in the Supporting Information). The conductivity shows the characteristic linear dependence on the gate voltage in the on-state, i.e.

$$\sigma(x,y) \approx \frac{[\mu_p c_{DL}](x,y)}{h_{sem}}\left[-V_{GS} + V_{TH}(x,y)\right]; \quad V_{GS} < V_{TH}(x,y) \quad (4)$$

where $[\mu_p c_{DL}](x,y)$ and $V_{TH}(x,y)$ are the local mobility–capacitance product and threshold voltage, respectively. **Table 1** shows the local mobility–capacitance product and threshold voltage obtained from this analysis for $V_{DS} = 0$ V at the four locations considered (see Figure S9 in the Supporting Information). Table 1 also shows for comparison the global values obtained from the analysis of the I–V characteristics with series resistance subtracted in Figure 1d,e.

Table 1. Local mobility–capacitance product and threshold voltages at four locations along scan line 4 indicated in Figure 2b, and global values.

Location	$[\mu_p c_{DL}]$ Product	V_{TH}
$Device_{\parallel\text{-Global}}$	1.9 μS V^{-1}	−0.51 V
$Source_{\perp\text{-Local}}$ (8, 4)	11.4 ± 0.3 nS V^{-1}	−0.38 ± 0.03 V
$Channel_{\parallel\text{-Local}}$ (31, 4)	9.3 ± 0.5 μS V^{-1}	−0.48 ± 0.07 V
$Channel_{\parallel\text{-Local}}$ (40, 4)	3.3 ± 0.1 μS V^{-1}	−0.48 ± 0.03 V
$Drain_{\perp\text{-Local}}$ (54, 4)	13.8 ± 0.3 nS V^{-1}	−0.47 ± 0.03V

The local threshold voltages show similar values to the one obtained from the macroscopic analysis of the I–V curve. However, the local mobility–capacitance product on the source and drain (which reflects the transverse conduction properties) is two orders of magnitude smaller than the ones obtained in the channel region (longitudinal conduction properties), reflecting quantitatively the anisotropic charge transport properties of the organic semiconducting material. The low mobility–capacitance product in the transversal direction could explain the relatively high source (access) resistance values obtained above in Figure 4c. On the other hand, the mobility–capacitance products for two different grains within the channel are similar, indicating that the grains' intrinsic transport properties are comparable. This result further supports the observation that at $V_{DS} = 0$ V, the semiconductor microstructure did not provide any contrast in Figure 3. With an applied drain voltage, the microstructure becomes visible due to a local potential drop at the grain boundary in the channel, giving to the grains different local gate potentials, and hence conductivities, thus limiting the charge carrier transport. The numerical analysis for the nonzero V_{DS} concurrently supports the observations (see Figure S9 in the Supporting Information). The effective longitudinal device mobility–capacitance product, with series resistance subtracted, ≈1.9 μS V^{-1} is 2–5 times lower than the one measured locally in the channel in the specific positions analyzed (see Table 1). Our previous work[14] reported a similar factor, and several possible explanations, although the exact origin of this quantitative discrepancy was not clear at that time. The extended data analysis of the potential maps obtained for all drain and gate voltages indicates that the origin of the reduction in

the effective longitudinal channel mobility–capacitance product is due to the decrease in effective channel mobility owing to the polycrystalline microstructure nature of the channel, see Figure S10 in the Supporting Information. This result again highlights the importance of nanoscale operando characterization in pinpointing charge transport bottlenecks.

The results presented in the present work can be extended, in principle, to other types of electrolyte-gated field-effect transistors (EGFETs) based on ion impermeable semiconductor materials, such as amorphous oxides, transition metal dichalcogenides, graphene, or nanotubes.[1] In all these cases, the electrolyte dielectric plays a crucial role in determining the device electrical performance, as it facilitates the migration of ions from the electrolyte to the semiconductor material interface, forming the electric double layer (EDL), which presents a very large capacitance (in the ≈μF cm^{-2} range). This large interfacial capacitance enables the modulation of the free charge carriers concentration in the semiconductor by the field effect with relatively low applied voltages (typically below 1 V), a significant advantage when dealing with biosensing and biorecording applications.[1–5] Electrolyte dielectrics also enable a fast enough response of EGFETs, leading to cutoff frequencies up to some kilohertz, essential for tailoring EGFETs to specific applications requiring relatively rapid switching (e.g., bioelectronic recordings). In-liquid SDM constitutes an ideal technique to probe the nanoscale electrical properties of EGFETs in operando, as it uses frequencies well beyond the cutoff frequency of the transistors and is sensitive to voltage variations of only the local semiconductor material conductivity. Other properties showing voltage dependencies, like the ionic diffusive interfacial capacitance of the EDL, are not directly probed, thus providing a relatively simple and transparent interpretation of the measurements, which is at the basis of the direct derivation of electric potential maps, essential to identify charge transport bottlenecks.

3. Conclusions

In summary, nanoscale operando characterization of EGOFETs has been performed in different operating regimes and for different microstructural signatures of the semiconducting thin film through a robust interpretation framework of in-liquid SDM that enabled quantitative local electric potential mapping of EGOFETs. Local electric potential maps have been extracted directly from the raw experimental data without requiring any prior calibration or numerical simulations, which constitutes a major advantage of the presented approach. The electric potential maps obtained under different biasing conditions provided direct information on the main charge transport bottlenecks present in the device. We showed that the device's macroscopic *I*–*V* characteristics are heavily dominated by the grain boundaries and series access resistance effects and, thus, do not reflect the true performance that can be achieved with this semiconducting material. The individual crystalline domains of the semiconducting material possess far better characteristics (reaching 40 S m^{-1} intrinsic conductivity); however, the less than 4 S m^{-1} effective conductivity observed from the global *I*–*V* characteristics indicates that the device is dominated by various bottlenecks. It thus demands developments of chemical design strategies that target improving the series access resistance and grain boundary characteristics instead of intrinsic charge carrier mobility of the semiconducting crystalline domains. In this regard, the relatively low transversal conductivity identified in the present study due to the anisotropic molecular packing[23,27] explains the relatively large series access resistance observed. Resolving the limitation induced by this molecular packing, for example, through molecular contact doping, as recently reported in OFETs,[8,30] could significantly improve the characteristics of devices based on this semiconducting material. Furthermore, increasing the grain sizes or decreasing the channel length would allow single grains connecting the source and drain electrodes and hence will reduce the impact of grain boundaries, and improve the device performance. The approach reported here opens new routes to obtain comprehensive quantitative insights into the charge carrier transport in electrolyte-gated transistors and pinpoint various bottlenecks. The straightforward approach to obtain quantitative electric potential maps from in-liquid SDM, which in principle cannot be obtained with the conventional KPFM technique in operando, is expected to provide an essential standard characterization methodology for probing charge transport mechanisms in electrolyte-gated transistors.

4. Experimental Section

Device Fabrication: Heavily doped n-type silicon wafers (purchased from Si-Mat) featuring thermal SiOx (200 nm) were employed. Source and drain electrodes (5 nm of Cr and 40 nm of Au) were fabricated by photolithography (MicroWriter ML Laser Lithography System) and thermal evaporation (System Auto 360 from BOC Edwards).[5,21] The electrodes were modified with a self-assembled monolayer of PFBT. Subsequently, a 2 wt% blend solution in chlorobenzene composed of diF-TES-ADT and PS in a ratio 4:1 was deposited on top of the substrates using the bar-assisted meniscus shearing technique at a rate of 10 mm s^{-1} and at 105 °C, as previously reported.[6,21] The semiconductor film entailed a very low number of complete molecular layers (around 3–5 monolayers).[9] Hence, in these films, there were no multilayers of crystals (with different internal grains) as often observed in evaporated thin films. Instead, the films prepared here consisted of a continuous polycrystalline thin film layer and, hence, with the optical microscopy images, one saw the crystalline domains of the whole film, not just the surface domains. The printing methodology employed to deposit the organic semiconductor layer ensured the preparation of highly homogeneous films with very high reproducibility[21] and improved performance and stability compared to the ones based on only the bare semiconductor.[5,21,22] Further details on the material preparation and fabrication process are provided elsewhere.[14,21]

Polarized Optical Microscopy: Optical microscope images were obtained using an Olympus BX51 equipped with a polarizer and analyzer at 90° in reflection mode.

Operando Local Characterization of EGOFETs by In-Liquid SDM: The nanoscale operando characterization of EGOFETs was done by in-liquid SDM following the principles originally presented in Ref. [31], further adapted to the specific case of EGOFETs in Ref. [14] and finally optimized in Ref. [20] (see Figure 1 therein). The measuring setup included automated functionalities and high throughput capabilities, as described in Ref. [20]. In a nutshell, it consisted of a JPK Nanowizard 4 BioAFM system mounted on a Nikon Eclipse optical microscope and integrating a point probe station (EverBeing EB-700) connected to an Agilent B2912A source measuring unit. The amplitude-modulated AC voltage of amplitude V_{ac}, electrical frequency in the range 1–30 MHz and modulating frequency of 2–10 kHz was applied by means of the Keysight 33622A function waveform generator, while the photodiode oscillation signal was processed with an external lock-in amplifier (eLockin 204/2, Anfatec). The use of frequencies in megahertz range (above the dielectric relaxation frequency of the electrolyte) prevented the screening of the applied AC potential by the ionic

diffusive interfacial layer and enabled obtaining local electrical information in electrolyte solutions. The use of lower frequencies resulted in a systematic loss of locality and the impossibility to obtain nanoscale electrical images (see Figure S11 in the Supporting Information). The operation of the setup was automated by using custom Python-based automated workflow running on an external computer.[20] The AFM data acquisition was done in advanced Quantitative Imaging (JPK) mode. HQ:NSC19/Cr–Au ($k \approx 1$ N m^{-1}, $f_{res} \approx 35$ kHz in liquid) and PPP-CONTSCPt ($k \approx 0.5$ N m^{-1}, $f_{res} \approx 10$ kHz in liquid) AFM tips were used as indicated in the respective figure captions. The data analysis of the measured electric force was performed using custom Python scripts that essentially generated relative electrostatic force curves by simply taking the relative changes of the recorded raw electrical oscillation amplitudes.[20] The use of relative electrostatic force values in the present work was motivated by the fact that the tip–sample system comprising a SDM probe with an EGOFET represented a dynamic impedance as a function of bias voltages and, due to operation at high frequency, this impedance also exhibited spatial variability as the probe traversed the source–channel–drain region, which could cause a measurement artefact by influencing the total applied tip–sample AC voltage, which was typically assumed to be constant. Previous approaches addressed this issue through renormalization factors.[14,26] However, applying the same method to a dynamic system like an EGOFET was impractical, primarily due to spatial variability mandating different factors for each electric force approach curve and for each operating point. Here, the robust and straightforward method was used to remove this artefact entirely during data processing introduced in Ref. [20], which involved simply taking the relative electrostatic force variation with respect to far-away reference tip–sample distance in an electric force approach curve, i.e., $(F_{el}|_{Z_{lift}} - F_{el}|_{Z_{ref}})/F_{el}|_{Z_{ref}}$, allowing fast qualitative and quantitative analysis (see Figure S12 in the Supporting Information for further details). The use of the relative electric force also eliminated the need for calibration and knowledge of various factors such as the cantilever spring constant, AFM optical system deflection sensitivity, lock-in amplifier gains, applied AC potential amplitude, and the renormalization factor. For obtaining potential maps from relative electrostatic force approach curves, a Python algorithm was developed that essentially implemented the process depicted in Figure S6 (Supporting Information).

For the local operando characterization of the EGOFETs, both an external gate electrode and the conductive tip of the SDM were used. The rationale behind this approach was to allow the flexibility of using the external gate electrode of any material to gate the transistor and not be limited by the availability of an appropriate AFM cantilever as in the previous implementation.[14] The use of two gate electrodes could shift the threshold voltage, but it did not affect the intrinsic performance or stability of the semiconducting material. Operando measurements were performed in a voltage range in which the EGOFET remained stable. The stable gate voltage window was from +0.2 to −0.8 V (step size = 0.02 V, # = 51) and drain voltage from 0 to −0.5 V (step size = 0.1 V, # = 6) covering all transport regimes, giving rise to 306 different operating points and electrical images (1 min 46 s per image). The simultaneously recorded drain current versus time measurements during operando in-liquid SDM were used to reconstruct an output curve (see Figure S13 in the Supporting Information and Figure 1d).

In-Liquid SDM Numerical Simulation: Local conductivity values were extracted by comparing the measured relative electric forces to the predictions of finite element numerical calculations. The physical model used, and its numerical resolution, were the same as those detailed in Ref. [14].

Author Contributions

S.R.-M. and M.M.-T. designed and fabricated the EGOFET devices. S.T. performed all the measurements and data analysis. S.T. conceived the idea of potential mapping, developed the algorithm and the interpretation framework. R.M.-S. developed and performed the numerical simulation. S.T., A.K., and G.G. wrote the paper with inputs from all the authors. A.K. and G.G. supervised and managed the project. All authors contributed to the final paper.

Supporting Information

Supporting Information is available from the Wiley Online Library or from the author.

Acknowledgements

This work had received funding from the European Union's Horizon 2020 research and innovation program under the Marie Skłodowska-Curie Grant Agreement No. 81386 (BORGES), from the European Horizon-EIC program under Grant Agreement No. 101046719 (PRINGLE) and by the Spanish Ministerio de Economıa, Industria y Competitividad, and the EU FEDER, through Grant Nos. PID2019-110210GB-I00 (BIGDATASPM) and PID2019-111682RB-I00 (GENESIS), and the "Severo Ochoa" Programme for Centers of Excellence in R&D (FUNFUTURE Grant Nos. CEX2019-000917-S and CEX2018-000789-S). The authors also acknowledge support from the Generalitat de Catalunya through Grant No. 2021SGR-00453 and the CERCA Program. G.G. acknowledges support from the ICREA Academia program. S.T. acknowledges the support from Joerg Barner (JPK) regarding automating the AFM operations. The authors would like to thank Prof. T. Cramer for providing the measurement software that allowed the macroscale *I–V* characterization of the EGOFETs.

Conflict of Interest

The authors declare no conflict of interest.

Data Availability Statement

The data that support the findings of this study are available from the corresponding author upon reasonable request.

Keywords

conduction anisotropy, conductivity maps, electrolyte-gated organic field-effect transistors, nanoscale, operando, operation regimes, potential maps, scanning dielectric microscopy

Received: September 20, 2023
Revised: November 21, 2023
Published online: December 24, 2023

[1] F. Torricelli, D. Z. Adrahtas, Z. Bao, M. Berggren, F. Biscarini, A. Bonfiglio, C. A. Bortolotti, C. D. Frisbie, E. Macchia, G. G. Malliaras, I. Mcculloch, M. Moser, T.-Q. Nguyen, R. M. Owens, A. Salleo, A. Spanu, L. Torsi, *Nat. Rev. Methods Primers* **2021**, *1*, 66.

[2] E. Genco, F. Modena, L. Sarcina, K. Björkström, C. Brunetti, M. Caironi, M. Caputo, V. M. Demartis, C. Di Franco, G. Frusconi, L. Haeberle, P. Larizza, M. T. Mancini, R. Österbacka, W. Reeves, G. Scamarcio, C. Scandurra, M. Wheeler, E. Cantatore, I. Esposito, E. Macchia, F. Torricelli, F. A. Viola, L. Torsi, *Adv. Mater.* **2023**, *35*, 2304102.

[3] E. Macchia, K. Manoli, B. Holzer, C. Di Franco, M. Ghittorelli, F. Torricelli, D. Alberga, G. F. Mangiatordi, G. Palazzo, G. Scamarcio, L. Torsi, *Nat. Commun.* **2018**, *9*, 3223.

[4] A. Kyndiah, M. Dipalo, A. Molazemhosseini, F. A. Viola, F. Modena, G. Iachetta, N. F. Zorn, F. J. Berger, J. Zaumseil, M. Caironi, F. De Angelis, *Sens. Actuators, B* **2023**, *393*, 134227.
[5] A. Kyndiah, F. Leonardi, C. Tarantino, T. Cramer, R. Millan-Solsona, E. Garreta, N. Montserrat, M. Mas-Torrent, G. Gomila, *Biosens. Bioelectron.* **2020**, *150*, 111844.
[6] F. Leonardi, S. Casalini, Q. Zhang, S. Galindo, D. Gutiérrez, M. Mas-Torrent, *Adv. Mater.* **2016**, *28*, 10311.
[7] S. Riera-Galindo, F. Leonardi, R. Pfattner, M. Mas-Torrent, *Adv. Mater. Technol.* **2019**, *4*, 1900104.
[8] J. Li, E. Colantoni, I. Temiño, P. Branchini, L. Tortora, M. Mas-Torrent, *Chem. Mater.* **2023**, *35*, 1527.
[9] A. Pérez-Rodríguez, I. Temiño, C. Ocal, M. Mas-Torrent, E. Barrena, *ACS Appl. Mater. Interfaces* **2018**, *10*, 7296.
[10] T. Cramer, A. Kyndiah, M. Murgia, F. Leonardi, S. Casalini, F. Biscarini, *Appl. Phys. Lett.* **2012**, *100*, 143302.
[11] P. Annibale, C. Albonetti, P. Stoliar, F. Biscarini, *J. Phys. Chem. A* **2007**, *111*, 12854.
[12] L. Balhorn, Q. Macpherson, K. C. Bustillo, C. J. Takacs, A. J. Spakowitz, A. Salleo, *Proc. Natl. Acad. Sci. USA* **2022**, *119*, 2204346119.
[13] J. Smith, W. Zhang, R. Sougrat, K. Zhao, R. Li, D. Cha, A. Amassian, M. Heeney, I. Mcculloch, T. D. Anthopoulos, *Adv. Mater.* **2012**, *24*, 2441.
[14] A. Kyndiah, M. Checa, F. Leonardi, R. Millan-Solsona, M. Di Muzio, S. Tanwar, L. Fumagalli, M. Mas-Torrent, G. Gomila, *Adv. Funct. Mater.* **2021**, *31*, 2008032.
[15] V. Palermo, M. Palma, P. Samorì, *Adv. Mater.* **2006**, *18*, 145.
[16] A. B. Naden, J. Loos, D. A. Maclaren, *J. Mater. Chem. C* **2014**, *2*, 245.
[17] T. Hallam, M. Lee, N. Zhao, I. Nandhakumar, M. Kemerink, M. Heeney, I. Mcculloch, H. Sirringhaus, *Phys. Rev. Lett.* **2009**, *103*, 256803.
[18] L. Collins, S. Jesse, J. I. Kilpatrick, A. Tselev, O. Varenyk, M. B. Okatan, S. A. L. Weber, A. Kumar, N. Balke, S. V. Kalinin, B. J. Rodriguez, *Nat. Commun.* **2014**, *5*, 3871.
[19] F. Mariani, F. Conzuelo, T. Cramer, I. Gualandi, L. Possanzini, M. Tessarolo, B. Fraboni, W. Schuhmann, E. Scavetta, *Small* **2019**, *15*, 1902534.
[20] S. Tanwar, R. Millan-Solsona, S. Ruiz-Molina, M. Mas-Torrent, A. Kyndiah, G. Gomila,in preparation.
[21] Q. Zhang, F. Leonardi, S. Casalini, I. Temiño, M. Mas-Torrent, *Sci. Rep.* **2016**, *6*, 39623.
[22] S. Ricci, S. Casalini, V. Parkula, M. Selvaraj, G. D. Saygin, P. Greco, F. Biscarini, M. Mas-Torrent, *Biosens. Bioelectron.* **2020**, *167*, 112433.
[23] R. Li, J. W. Ward, D.-M. Smilgies, M. M. Payne, J. E. Anthony, O. D. Jurchescu, A. Amassian, *Adv. Mater.* **2012**, *24*, 5553.
[24] L. Huetter, A. Kyndiah, G. Gomila, *Adv. Theory Simul.* **2023**, *6*, 2200696.
[25] Q. Zhang, A. Tamayo, F. Leonardi, M. Mas-Torrent, *ACS Appl. Mater. Interfaces* **2021**, *13*, 30902.
[26] R. Millan-Solsona, M. Checa, L. Fumagalli, G. Gomila, *Nanoscale* **2020**, *12*, 20658.
[27] S. Hunter, T. D. Anthopoulos, *Adv. Mater.* **2013**, *25*, 4320.
[28] W. Shockley, *Proc. IRE* **1952**, *40*, 1365.
[29] R. Rödel, *PhD Degree Thesis*, EPFL Lausanne **2016**.
[30] J. Li, A. Babuji, L. Fijahi, A. M. James, R. Resel, T. Salzillo, R. Pfattner, C. Ocal, E. Barrena, M. Mas-Torrent, *ACS Appl. Mater. Interfaces* **2023**, *15*, 5521.
[31] G. Gramse, M. A. Edwards, L. Fumagalli, G. Gomila, *Appl. Phys. Lett.* **2012**, *101*, 213108.